Fuel 423 (2026) 139263

Contents lists available at ScienceDirect

Fuel

journal homepage: www.elsevier.com/locate/fuel

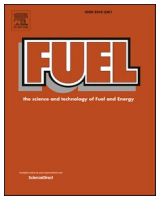

Full Length Article

Unlocking the Size-Dependent mechanism of CO_2 reduction on Carbon-Supported Ni_n clusters

Yimeng Sun [a], Lin Tao [a,*], Meixu Lu [a], Xin Quan [a], Mingjie Wu [b,*], Javed Rehman [c], Nan Wang [a,*], Lixiang Li [a], Baigang An [a]

[a] School of Chemical Engineering, University of Science and Technology Liaoning, Anshan 114051, China
[b] State Key Laboratory of New Textile Materials and Advanced Processing, Wuhan Textile University, Wuhan 430200, China
[c] State Key Laboratory of Metastable Materials Science and Technology, Yanshan University, Qinhuangdao 066004, China

ARTICLE INFO

Keywords:
CO_2 reduction
DFT
Single-atom catalyst
Cluster
Active site density

ABSTRACT

The precise size control of metal nanoclusters represents a frontier in catalysis, as their atomically defined structures give rise to electronic structures intermediate between larger nanoparticles and bulk materials. Herein, we introduce a strategic approach utilizing carbon-supported, size-specific nickel nanoclusters, ranging from single atoms to pentamers, high-value-added fuels are produced through efficient electrochemical conversion of CO_2. We systematically evaluated the CO_2 reduction reaction (CO_2RR) performance of these catalysts through comprehensive density functional theory (DFT) calculations. Crucially, our work pioneers the application of molecular dynamics simulations, combined with electronic structure and charge density analysis, to confirm the exceptional stability of the SA@Ni_x (x = 1–5) configurations. SA@Ni_3 and SA@Ni_4 have been confirmed as candidate materials, which both are respectively proficient in the formic acid and CO pathways and can effectively inhibit HER side reactions. The product distribution is elucidated by the regulatory function of the center of the d band position. We demonstrate that both SA@Ni_3 and SA@Ni_4 possess low limiting potentials and optimal intermediate adsorption strengths, underpinning their superior performance. This study clarified the correlation between the structure and performance of cluster catalysts at the atomic scale, laying a theoretical foundation for the rational design of efficient SACs and cluster catalysts.

1. Introduction

Global climate mitigation strategies encompass two complementary approaches, reducing CO_2 emissions through energy efficiency and low-carbon energy sources, and deploying negative emissions technologies (NETs) to actively remove atmospheric CO_2 [1,2]. While emission reduction remains paramount, NETs are increasingly essential for achieving climate targets, particularly for hard-to-abate sectors where conventional carbon capture and storage is impractical. With global CO_2 emissions exceeding 51 billion tons annually and fossil fuels supplying 63.1% of energy—rising to 85% in developing economies by 2050—the development of low-cost, widely applicable NETs has become urgent. Among emerging NET strategies, electrocatalytic CO_2 reduction stands out as a promising approach to convert captured CO_2 into valuable fuels and chemicals, simultaneously addressing carbon removal and sustainable energy production. However, breaking the strong C=O bonds in CO_2 requires high activation energy, making the process challenging. Existing electrocatalysts still struggle with stability, reaction rate, overpotential, current density, and selectivity, limiting their efficiency [3–5]. Developing better catalysts to enhance CO_2RR performance is essential.

In electrocatalysts, active metals directly participate in the catalytic reaction, and their coordination environment considerably affects the electronic structure, thereby determining the catalytic activity [6]. However, understanding coordination effects in heterogeneous catalysts remains challenging because of their ill-defined surface structures. As a typical model catalytic system, single-atom catalysts (SACs) feature well-defined and accessible active sites, making them an ideal platform for exploring surface coordination chemistry [7]. SACs anchor metal active centers stably on the support surface through coordination bonds, allowing the modulation of electrocatalytic activity and selectivity via strong metal-support interactions [8]. Featuring outstanding catalytic

* Corresponding authorsat: School of Chemical Engineering, University of Science and Technology Liaoning, Anshan 114051, China, State Key Laboratory of New Textile Materials and Advanced Processing, Technologies, Wuhan Textile University, Wuhan 430200, China.
E-mail addresses: taolin@ustl.edu.cn (L. Tao), mjwu@wtu.edu.cn (M. Wu), chlwangnan@126.com (N. Wang).

https://doi.org/10.1016/j.fuel.2026.139263
Received 4 November 2025; Received in revised form 22 February 2026; Accepted 23 March 2026
Available online 27 March 2026

performance and maximum atom utilization, SACs have been widely applied and recognized as highly efficient catalysts. In particular, metal atoms (M = Fe, Co, Ni, Cu) anchored in two-dimensional carbon materials in the form of $M-N_4-C$ structures have emerged as promising electrocatalysts for the CO_2RR [9–17]. For instance, Xie et al. [11] reported that Ni SACs with N_4 coordination supported on N-doped carbon display superior activity and stability toward CO_2RR. The coordination configuration and bonding nature of SACs are crucial for optimizing their catalytic performance. Nevertheless, SACs suffer from a lack of adjacent active sites, limiting their performance in reactions that require multiple neighboring sites. To address this issue, it is meaningful to explore whether the uniform distribution of metal–metal bonded nanoclusters near single-atom sites can boost the CO_2RR catalytic activity while preserving high metal atom utilization [18].

Nanoparticles (NPs) are widely used as alternatives to traditional bulk metal catalysts. They offer high activity, excellent selectivity, and low cost [19–23]. Nanoclusters, which typically contain fewer than 150 atoms, and sub-nanoclusters, usually composed of fewer than 30 atoms, exhibit strong quantum confinement effects. These effects lead to unique electronic states and catalytic performance. Their well-defined atomic structures set them apart from larger nanoparticles and bulk materials [23,24]. Due to their tunable size, composition, and geometry, as well as their low coordination site density and high specific surface area, sub-nanoclusters show great potential in nanocatalysis. Their catalytic properties often emerge from atomic-scale features and can change dramatically with the addition or removal of a single atom. Metal nanoclusters with atomic-level precision have opened a new frontier in electrocatalysis research [25–27], They can be synthesized with molecular purity and have structures determined by crystallography [28,29], enabling clear investigation of structure–property relationships.

Recent studies have shown that reducing nanoparticle size to the nanocluster regime significantly improves atomic utilization efficiency. Various metallic nanoparticles, including Cu, Ni, Au, Ag, Bi, Pd, and Sn, have been investigated [30–36]. These findings consistently indicate that nanoparticle size governs both CO_2RR activity and product selectivity. In general, nanoparticles exhibit higher CO_2RR activity than bulk metal surfaces. Specific metal nanoclusters can effectively bridge uncoordinated metal atoms, enabling efficient CO_2-to-CO conversion. These clusters exhibit both high reactivity and excellent stability. They maintain high CO current density and faradaic efficiency over extended periods, ensuring the continuous and efficient progression of the catalytic process [12,37]. Metal nanoclusters can function either as active centers or as supports for SACs. In doing so, they further enhance the overall catalytic performance. The combination of metal nanoclusters with SACs creates a synergistic effect. This synergy improves both catalytic activity and stability, opening new possibilities for efficient catalysis [38–42]. This integration also helps address the individual limitations of each material. Some metal nanoclusters exhibit high activity but suffer from poor stability. In contrast, SACs offer excellent stability but limited activity. By combining the two, the resulting catalyst achieves significantly enhanced stability while retaining high activity. This approach extends the catalyst's service life and provides a more reliable option for practical applications.

Isolated atoms and ultrafine clusters demonstrate remarkable catalytic performance as CO_2RR catalysts. However, the influence of metal content on the structure–activity relationship of these catalysts remains insufficiently understood. Therefore, a systematic investigation into how metal atoms and their quantities affect catalytic behavior is essential. Such fundamental understanding is critical for developing rational strategies to design low-cost and efficient catalysts.

Recent years have seen great advances in CO_2 conversion catalysis. Noble metal catalysts (Pt, Pd, Au, etc.) show high CO_2 hydrogenation performance but suffer from high cost and sintering, spurring the search for earth-abundant alternatives [43]. Ni_n transition metal clusters are promising candidates, with DFT confirming their size and electronic structure jointly regulate CO_2 activation [44]. However, relevant studies focus only on discrete sizes (n = 2–6, 8) and activation energetics, ignoring product selectivity. Atomically precise coinage metal nanoclusters have realized precise size/ligand control [45], yet such research is dominated by Au and Ag systems. Besides, electronic metal-support interactions enable Ag nanoparticles to achieve nearly 100% CO Faradaic efficiency [46], and tailored Cu clusters on defective supports selectively produce methane via the *COOH pathway [47]. Despite these advances, the mechanistic origin of size-dependent selectivity in earth-abundant transition metal clusters—especially how intrinsic size modulates the CO/HCOOH pathway competition—remains unquantified.

The selection of Ni_1-Ni_5 clusters as the research focus is grounded in the unique scientific significance of this size regime, which encompasses the complete structural transition from single atoms (Ni_1) to sub-nanometer clusters (Ni_2-Ni_5) while maintaining relatively low structural complexity. This size range exhibits pronounced size-dependent catalytic behavior extensively documented in both theoretical and experimental literature [48,49]. Notably, Ni_5 represents the critical threshold for the two-dimensional to three-dimensional structural transition, with clusters larger than five atoms tending to form complex 3D configurations that substantially increase computational and experimental complexity [50,51]. Within the Ni_1-Ni_5 regime, catalytic performance in CO_2 reduction demonstrates stepwise evolution with increasing atomic number: single-atom Ni_1 achieves optimal CO selectivity with Faradaic efficiency up to 97%, while Ni_2-Ni_5 clusters enable product switching (e.g., Ni_4 favoring CH_4 production) and syngas ratio tuning, with performance extremum also observed in HER, OER, and ORR. Beyond five atoms, size sensitivity diminishes and competing reactions such as HER become more pronounced [52]. Therefore, the Ni_1-Ni_5 series constitutes an ideal model system for elucidating the fundamental correlations among geometric structure, electronic configuration, and catalytic performance.

In this work, we construct a series of metal clusters into atomic-level precise theoretical models, ranging from single atoms to Ni_x (x = 1–5) clusters supported on carbon substrates, to systematically evaluate their efficacy as electrocatalysts for CO_2RR. Our computational methodology commenced with a rigorous assessment of structural stability and electronic properties via *ab initio* molecular dynamics (AIMD) and density of states (DOS) analysis. We subsequently probed the critical initial stages of catalysis, including CO_2 adsorption, activation, and the competitive adsorption against HER. To unravel the reaction pathways and origin of selectivity, the thermodynamic and electronic structure characteristics of the reaction path were determined through the calculation of Gibbs free energy and limiting potential as well as Crystal Orbital Hamiltonian Population (COHP) analysis. This multi-faceted investigation not only deciphers the structure–activity-selectivity relationships in SA@Ni_x catalysts but simultaneously providing a transferable theoretical framework toward the development of next-generation, carbon-supported cluster catalysts.

2. Computational details

The theoretical analysis and all calculations of the study using the DMol^3 module based on the first principles of DFT, with a focus on exploring the adsorption characteristics of CO_2 on the SA@Ni_x monolayer [53,54]. The Perdew-Burke-Ernzerhof (PBE) functional, specifically its density-dependent (density-dependent GGA approximation) is selected as the method to describe the exchange correlation effect [55,56]. To precisely describe van der Waals interactions, all calculations were carried out using TS's DFT-D method, as weak interactions cannot be accurately described by standard PBE functionals [57]. In order to make the calculation result of total energy more accurate, spin polarization is introduced in the calculation and DFT correction is carried out. Strict convergence criteria (energy, 10^{-5} eV, force, 0.05 eV/ A) were set in the calculation, and a 3 × 3 × 1 K-point grid centered on

point γ was adopted. To isolate the periodic mirror image interaction, the vacuum layer of 20 Å was added in the vertical direction, and all atoms were relaxed during the optimization process. An implicit solvation model was employed to represent the solvent, with the dielectric constant set to 78.4 for water.

It should be noted that the present calculations are based on a periodic DFT framework with an implicit solvation treatment and without explicit electrode potential control. Although such approximations may influence the absolute free energy values and predicted overpotentials, they are widely adopted in theoretical CO_2RR studies and have been demonstrated to reliably capture relative trends in adsorption energetics and reaction pathways. Therefore, the mechanistic insights and comparative catalytic trends discussed here are expected to remain qualitatively valid, while quantitative predictions may require more advanced approaches incorporating explicit solvent dynamics and constant-potential simulations.

Furthermore, AIMD simulations were performed to evaluate the thermal stability of the catalysts at finite temperature, complementing static DFT optimizations. While static DFT calculations identify minimum-energy structures, AIMD captures dynamic structural fluctuations and provides a more realistic assessment of stability. COHP analysis was employed to quantify bonding and antibonding interactions, enabling a deeper understanding of electronic structure contributions to catalytic activity. It should be noted that density functional theory, particularly within the PBE functional, may introduce systematic errors in describing electron correlation and temperature-dependent effects. Although absolute energies may be affected, the relative trends and mechanistic insights discussed here are expected to remain reliable within the adopted computational framework.

3. Results and discussion

3.1. Structural stability

In this part, we designed a novel single-atom synergistic cluster catalyst supported on graphene doped with transition metal Ni single atoms. As shown in Fig. 1 **a**, the model consists of a graphene monolayer containing 66 carbon (C) atoms and 4 nitrogen (N) atoms, which serves as a stable support for the catalyst. The detailed structure is illustrated in **Fig. S1**. To maximize catalytic activity, a single nickel atom is precisely

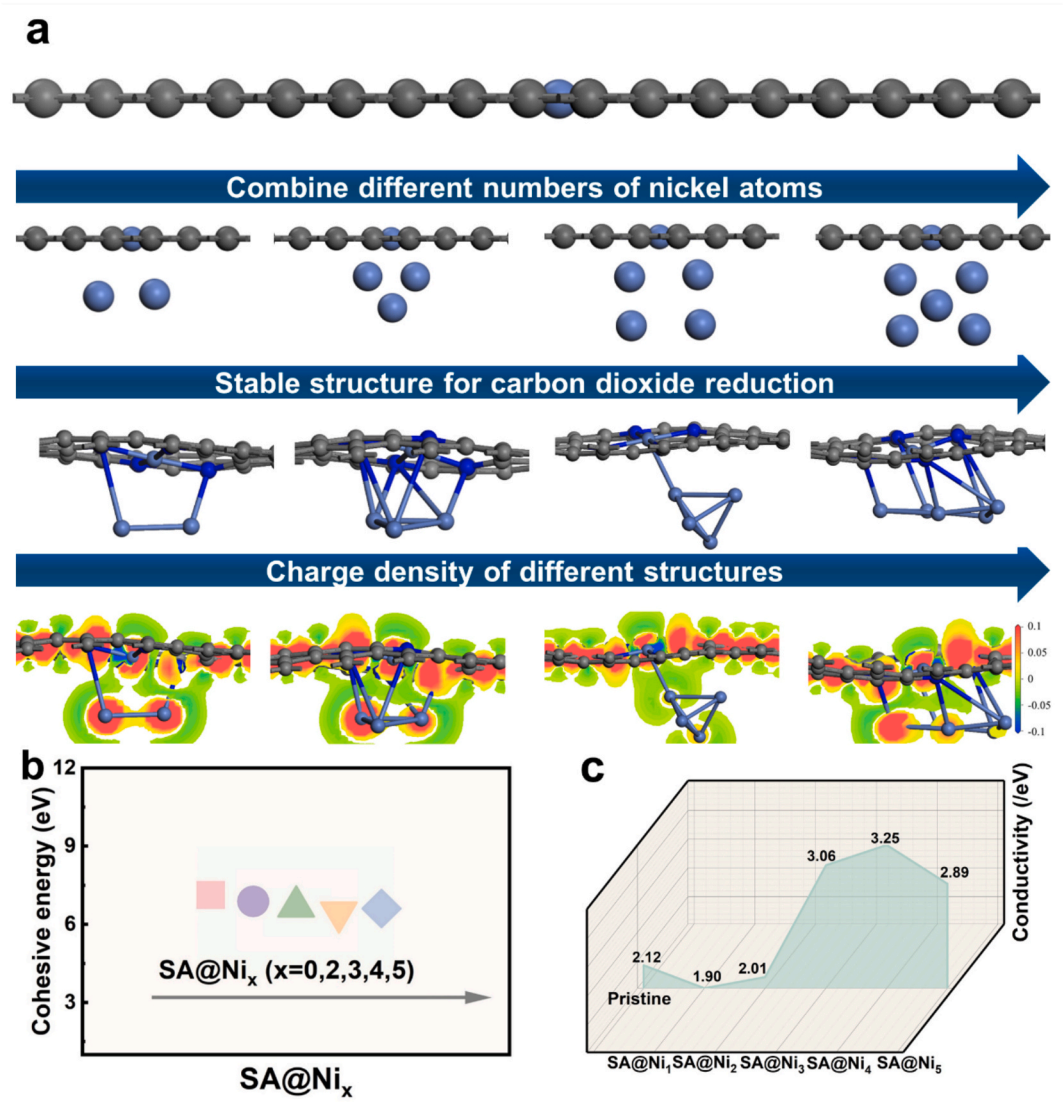

Fig. 1. Structural and electronic properties of SA@Ni$_x$ monolayers. (a) Optimized structures (upper) and charge density difference maps (lower) of SA@Ni$_x$ (x = 1–5); yellow and cyan isosurfaces indicate electron accumulation and depletion, respectively, revealing charge redistribution upon cluster formation. (b) Cohesion energy of SA@Ni$_x$ monolayers; more negative values indicate higher thermodynamic stability, with Ni$_4$ and Ni$_5$ showing comparable stability. (c) DOS at the Fermi level; higher values correlate with enhanced metallic character and catalytic activity, where Ni$_3$ and Ni$_4$ exhibit elevated DOS favorable for CO_2 reduction.

anchored onto the upper surface of graphene, while additional Ni atoms remain suspended below the graphene layer. This configuration preserves overall structural stability and enhances catalytic efficiency. Specifically, the Ni atom directly bonded to the graphene surface forms strong coordination bonds with four adjacent N atoms. This coordination further reinforces the structural stability of the catalyst through a strong metal-support interaction.

To determine whether the differences in catalytic performance are determined by the Ni metal content, we systematically optimized the graphene surfaces with different Ni loading amounts, as shown in Fig. 1 **a**. Subsequently, the stability of the SA@Ni_x structure was evaluated through combined energy calculations and charge density analysis. Additionally, AIMD simulations were conducted to assess the stability of the structure under operating conditions. Finally, the DOS of SA@Ni_x and the original graphite monolayer were quantified, which served as a key indicator for the catalyst's electrical conductivity.

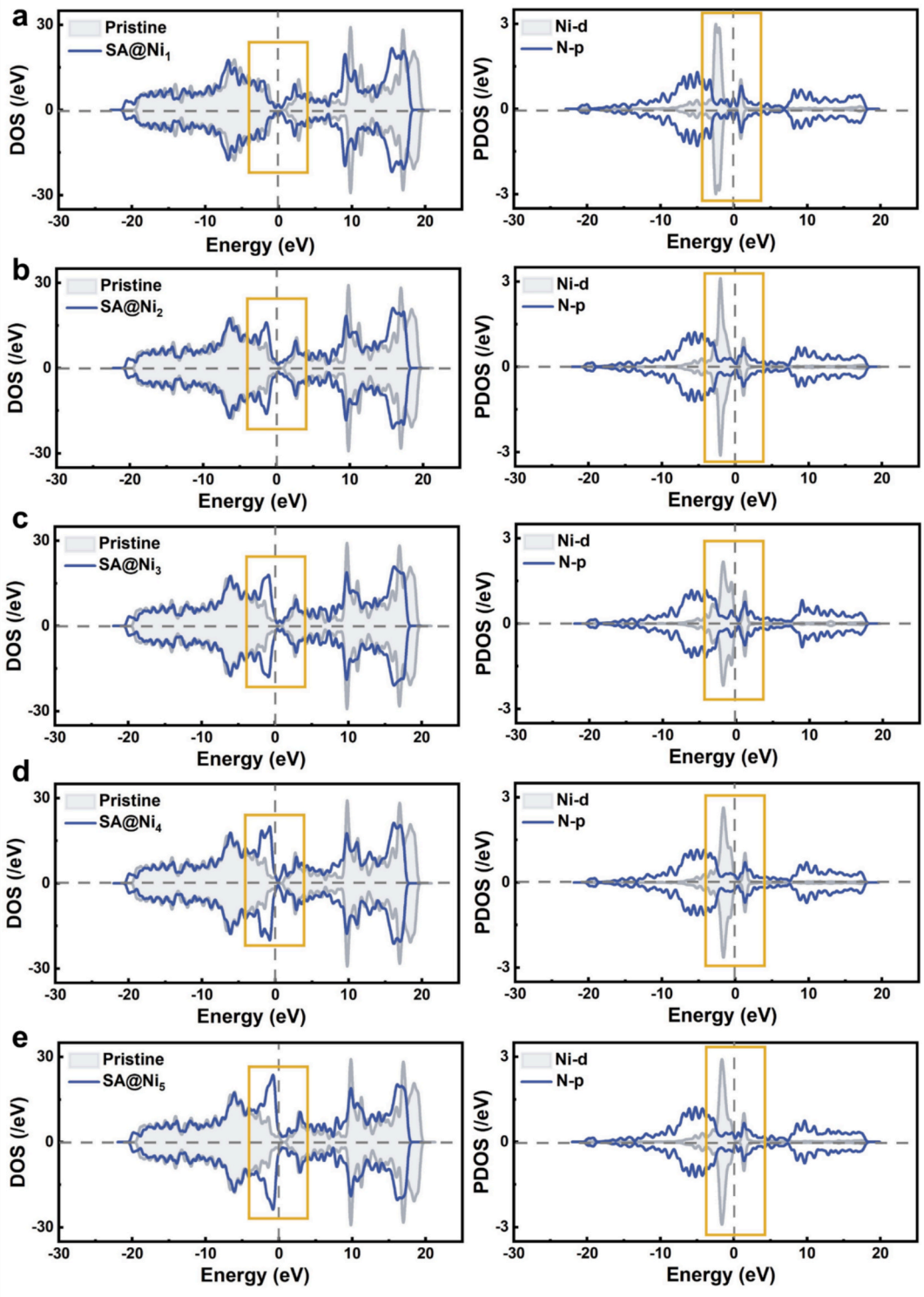

Fig. 2. The density of states of (a) SA@Ni_1, (b) SA@Ni_2, (c) SA@Ni_3, (d) SA@Ni_4, and (e) SA@Ni_5.

High stability is essential for the practical application of catalysts. In the SA@Ni_x system, this stability is directly indicated by the cohesive energy, with larger values corresponding to enhanced structural stability [58–60]. The cohesion energy (E_{coh}) is defined by the following formula [61]:

$$E_{coh} = \frac{n_1 E_{TM} + n_2 E_C + n_3 E_{N-} E_{C2N}}{n_1 + n_2 + n_3} \quad (1)$$

Here E_C and E_N represent the energies (in eV) of C and N atoms, respectively. n_1, n_2, and n_3 correspond to the numbers of metal, C, and N atoms. Fig. 1 **b** presents the calculated cohesive energies for the SA@Ni_x structures. The results indicate that these structures are less stable than the pristine graphene monolayer (−9 to −10 eV/atom) but exhibit greater stability than phosphorene (4.12 to 6.45 eV/atom) and silicene (3.71 eV/atom) [62]. (Refer to **Table S1** for detailed data) Therefore, these results illustrate the substantial stability of all SA@Ni_x configurations.

To investigate the interaction between the nickel and the graphene monolayer, charge density analysis was performed on the SA@Ni_x system. As shown in Fig. 1 **a**, the charge distribution reveals a depletion of electron density around the nitrogen atoms and an accumulation around the metal atoms. This indicates a net electron transfer from the nickel atoms to the underlying N-doped graphene support. The resulting interaction stabilizes the bond between the Ni atoms and the adjacent nitrogen atoms. To further assess the thermodynamic stability of the SA@Ni_x structures, AIMD simulations were conducted. The simulations were performed at 500 K for a total of 10 ps, with structural snapshots recorded every 10 fs. The results, detailed in **Fig. S2**, confirm that the materials exhibit excellent structural stability under the simulated conditions.

Finally, the electrical conductivity of the catalyst was evaluated by examining the DOS at the Fermi level [61,63–65]. The DOS serves as a key indicator of a material's conductive properties. As shown in Fig. 1 **c**, the SA@Ni_x structure exhibits a higher DOS at the Fermi level compared to pristine graphene. This enhancement suggests that the incorporation of Ni species significantly improves the catalytic performance. Detailed calculation results are provided in Fig. 2.

The introduction of Ni notably enhances the total DOS near the Fermi level, indicating improved charge transport properties in the SA@Ni_x system. To gain further insight, projected density of states (PDOS) analysis was performed to reveal the electronic properties of the Ni-doped. A pronounced overlap is observed between Ni and N states, signifying strong Ni-N coupling. This strong interaction enables Ni to bind firmly to the graphene monolayer. The resulting bonds between the Ni atoms and the substrate therefore ensure the structural stability of the catalyst.

3.2. Activity and selectivity

To understand the catalytic mechanism and advantages for CO_2RR, we evaluated the d-band center and CO_2 activation degree. Reaction pathway selectivity was explored by calculating the free energy changes of key intermediates (*COOH and OCHO) relative to H. Promising SA@Ni_x catalysts were further screened to ensure optimal CO_2RR performance. Finally, the diffusion behavior of CO_2 on different material surfaces was assessed by computing diffusion coefficients using molecular dynamics simulations.

CO_2 adsorption constitutes the first and critical step in the CO_2RR process, with stable adsorption serving as a prerequisite for the subsequent reaction. The degree of CO_2 activation can, to some extent, reflect the catalytic performance. As demonstrated in **Fig. S3 and S4**, which presents the three-dimensional configuration of adsorbed CO_2, the catalyst surface exhibits stable CO_2 adsorption capacity. Accordingly, the molecular geometry of CO_2 undergoes significant distortion, indicating its preliminary activation.

To further elucidate the activation level, electrical conductivity, and charge transfer behavior during the interaction between CO_2 and the SA@Ni_x surface, charge density difference and DOS analyses were performed, with results also presented in **Fig. S3 and S4.** The results reveal substantial charge transfer within the SA@Ni_x-CO_2 adsorbed system. The prominent red region surrounding CO_2 clearly indicates electron donation from SA@Ni_x to CO_2, confirming a strong interaction between the two species. Moreover, the p-d orbital interaction involving CO_2 and the transition metal in SA@Ni_x further corroborates this electronic coupling. For quantitative assessment, key parameters—including CO_2 adsorption energy, optimized bond lengths, and bond angles—are detailed in **Table S2**. A reduction in the O-C-O bond angle is directly correlated with an enhanced degree of CO_2 activation. Specifically, the C-O bond lengths range from 1.22 to 1.30 Å, while the O-C-O bond angles vary between 131.58° and 165.85° (Fig. 3 **b**). These geometric distortions collectively demonstrate the effective activation of CO_2 on the SA@Ni_x surface.

The interaction between CO_2 and Ni atoms was characterized using the d-band center model. This approach reveals the adsorption mechanism of CO_2 on the catalyst surface. As shown in Fig. 3 **a**, the adsorption energy of SA@Ni_x exhibits a linear correlation with the d-band center. This correlation is in good agreement with the predictions of the theoretical d-band model. The upshifted d-band center of Ni_3 leads to stronger *CO adsorption, favoring the CO pathway, while the downshifted d-band of Ni_5 weakens *COOH binding, steering selectivity toward HCOOH. This consistency suggests that the upward shift of the anti-bonding orbital enhances the adsorption energy.

The HER is kinetically more favorable and thus competes with CO_2RR. An effective catalyst must therefore suppress HER to enable efficient CO_2 reduction. We first examined HER through H_2O adsorption, as CO_2RR typically operates in neutral or alkaline electrolytes. As shown in **Table S1 and S2**, the adsorption energy of H_2O is consistently lower than that of CO_2 on all SA@Ni_x surfaces. This indicates that CO_2 binds more strongly than H_2O, allowing CO_2 to occupy the initial active sites and thereby inhibit HER. During the early protonation stage, CO_2 hydrogenation proceeds via two key intermediates, *COOH and *OCHO. Fig. 3 **c** compares the free energies of *COOH, *OCHO and *H. Both SA@Ni_3 and SA@Ni_4 lie in the lower right quadrant, the region associated with CO_2RR selectivity. This indicates a thermodynamic preference for *COOH or OCHO formation over H.

Together, these findings demonstrate that SA@Ni_3 and SA@Ni_4 selectively promote CO_2RR while effectively suppressing HER under electrochemical conditions.

CO_2 mass transfer on the catalyst surface limits the reaction rate in this system [66,67]. To evaluate practical catalytic performance, we calculated the diffusion coefficients of CO_2 on different material surfaces using molecular dynamics simulations. **Figs. S5 and S6** show the equilibrium adsorption configurations of CO_2 on all catalysts. We first computed the mean square displacement (MSD) for each SA@Ni_x structure, as presented in Fig. 3 **d**. The results indicate that SA@Ni_4 initially exhibits the lowest diffusion activity. We then applied Einstein's diffusion equation to derive the diffusion coefficients, which are summarized in **Table S4**. SA@Ni_4 shows the optimal diffusion performance, with a diffusion coefficient of 1.44×10^{-8} m^2/s. Notably, the diffusion coefficient governs CO_2 surface diffusion. A smaller diffusion coefficient corresponds to more stable CO_2 adsorption, which in turn leads to superior catalytic performance.

3.3. CO_2 reduction to CO or HCOOH

We calculated the free energies of key intermediates involved in the CO and HCOOH pathways for CO_2 reduction. On this basis, we systematically evaluated the free energy changes along the entire reaction pathway. On SA@Ni_x surfaces, CO_2 conversion proceeds through two distinct pathways. It can be reduced to CO via the COOH intermediate or to HCOOH via the OCHO intermediate. Fig. 4 presents the free energy

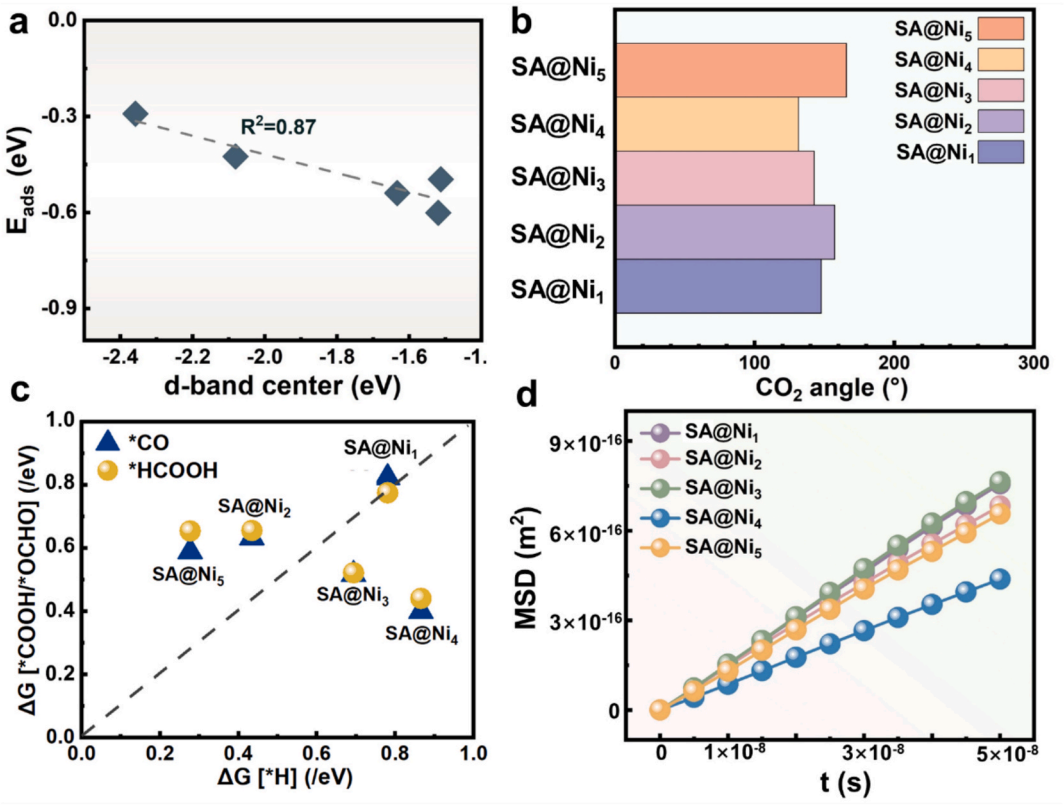

Fig. 3. Mechanistic analysis of CO_2 reduction on SA@Ni_x. (a) Linear correlation between d-band center and CO_2 adsorption energy; Ni_3 and Ni_4 exhibit optimal d-band positions. (b) CO_2 activation angle (O-C-O bending); smaller angles on Ni_3 and Ni_4 indicate stronger activation. (c) Free energy diagram for CO_2RR vs. HER; lower barriers for *COOH/*OCHO than *H on Ni_3/ Ni_4 explain their high selectivity. (d) CO_2 diffusion barriers; moderate barriers on Ni_3/ Ni_4 balance reactant supply and surface residence time.

profiles for CO and HCOOH formation from CO_2 through the two-electron pathway on SA@Ni_x. The corresponding limiting potentials and overpotentials are also illustrated schematically.

We calculated Gibbs free energy profiles to determine the rate-determining steps and energy barriers for CO_2 reduction to CO and HCOOH on different catalysts. For the CO path, the speed decision step of SA@Ni_1 is determined to be CO desorption, with an energy barrier as high as 1.14 eV. After the introduction of Ni clusters, the rate-determining step of SA@Ni_2 remains CO desorption, but the energy barrier is reduced to 0.78 eV. The speed determination steps of SA@Ni_3, SA@Ni_4 and SA@Ni_5 were all transformed into *COOH → *CO steps, and the energy barriers of the three were controlled at 0.68 eV, 0.50 eV and 0.78 eV respectively. Among them, the energy barrier of SA@Ni_4 is pushed to the minimum, indicating that its CO generation activity is optimal. For the HCOOH path, the speed decision step of SA@Ni_1 is HCOOH desorption, with an energy barrier of 1.04 eV. The speed-determining steps of SA@Ni_2 and SA@Ni_5 were determined to be OCHO → HCOOH, with energy barriers of 0.86 eV for both. The speed-up step of SA@Ni_3 is HCOOH → HCOOH, and the energy barrier drops to 0.66 eV. The energy barrier of SA@Ni_4 in this path is pushed up to 1.37 eV, and its speed decision step is *OCHO → *HCOOH. Among them, the energy barrier of SA@Ni_3 is suppressed to the lowest level and is regarded as the best catalyst for generating HCOOH.

3.4. Catalytic performance

To quantitatively compare catalytic activity, Fig. 4 **c and 4d** show the limiting potential (U_L) and overpotential (η) for CO_2 reduction to CO and HCOOH on SA@Ni_x. Compared with other single-atom and multi-atom catalysts, SA@Ni_3 and SA@Ni_4 exhibit superior catalytic performance with lower overpotentials. Overpotential is a key parameter that determines the energy consumption of the electrochemical reaction. Excessively strong adsorption energy can substantially reduce reaction efficiency. Therefore, correlating overpotential with product adsorption energy provides insight into the structure–performance relationship of the catalyst.

Fig. 5 **a** shows that during the carbon dioxide generation process, SA@Ni_4 performed the best, with an overpotential of only 0.50 V. This indicates that it has excellent catalytic activity and lower energy consumption. The peak of the volcano plot corresponds to the medium adsorption energy of the product, and this energy value can produce the best catalytic effect.

As shown in Fig. 5 **b**, SA@Ni_3 demonstrated the best overall performance in synthesizing HCOOH. The overpotential for HCOOH generation was 0.66 V, indicating that moderate adsorption is beneficial for achieving a high HCOOH yield. When |η| exceeds 0.9 V, this reaction requires a large amount of energy input, and therefore is unlikely to proceed.

This analysis indicates that CO_2RR catalyzed by SA@Ni_x is feasible. While SA@Ni_3 and SA@Ni_4 become the best catalysts for achieving high CO_2RR performance.

Our study investigates the outstanding performance of SA@Ni_x for electrocatalytic deep hydrogenation of CO_2 at low electrode potentials. For CO and HCOOH production, SA@Ni_4 and SA@Ni_3 exhibit the best catalytic performance, respectively. These results demonstrate the great potential of graphene monolayers doped with Ni single atoms and Ni clusters for CO_2RR. Accordingly, SA@Ni_4 and SA@Ni_3 are identified as the best-performing catalysts for CO_2 reduction in this study.

3.5. Catalytic mechanism

To understand why SA@Ni_3 and SA@Ni_4 exhibit the best catalytic

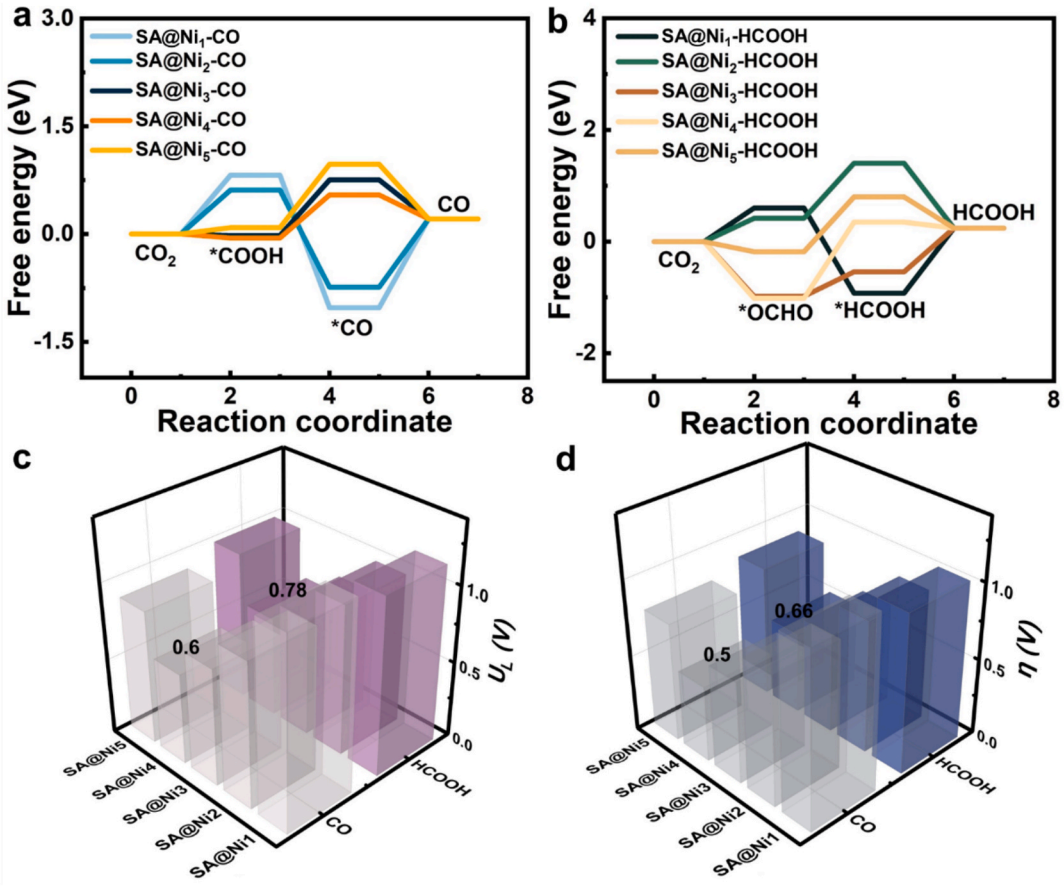

Fig. 4. Energetics and selectivity of CO_2 reduction on SA@Ni_x. (a) Gibbs free energy for CO pathway; Ni_4 shows the lowest barrier. (b) Gibbs free energy for HCOOH pathway; Ni_3 is most favorable. (c) Limiting potentials for CO and HCOOH; Ni_4 and Ni_3 require the lowest overpotentials, respectively. (d) Overpotentials confirming Ni_3 and Ni_4 as optimal catalysts for HCOOH and CO production.

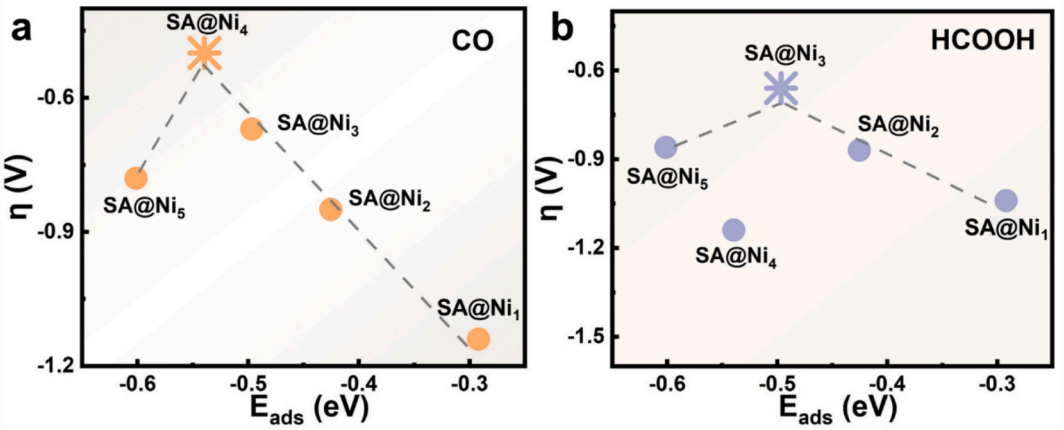

Fig. 5. Overpotential on SA@Ni_x determined by product adsorption energy. (a) CO adsorbed on the SA@Ni_x. (b) HCOOH adsorbed on the SA@Ni_x.

performance, we analyzed the interaction between key intermediates and the catalytic active sites from a molecular orbital perspective. Previous studies have shown that bonding orbitals at the active site dominate the adsorption process [68–73]. An optimal interaction should be balanced. If the interaction is too strong, it increases the reaction barrier for subsequent steps and becomes rate-limiting. If the interaction is too weak, it reduces catalytic efficiency and may render the catalyst inactive. Therefore, moderate interaction strength is essential for achieving high-performance catalysis. We performed COHP analysis to examine the interaction between intermediates and the active sites on SA@Ni_3 and SA@Ni_4.

Fig. 6 shows the distribution of bonding and antibonding orbitals of SA@Ni_3 and SA@Ni_4 with gas atoms near the Fermi level, with the corresponding integrated crystal orbital Hamilton population (ICOHP) values (in absolute terms) plotted. The ICOHP values reflect the bond strength the interaction between Ni and C atoms. For CO production, the ICOHP value on the SA@Ni_4 catalyst surface is 0.71 eV, and on the SA@Ni_3 catalyst surface it is 0.81 eV,. As shown in **Figs. S7**, on the SA@Ni_1 catalyst surface, the ICOHP value the Ni-C interaction is 0.41 eV, on the SA@Ni_2 catalyst surface it is 0.57 eV, and on the SA@Ni_5

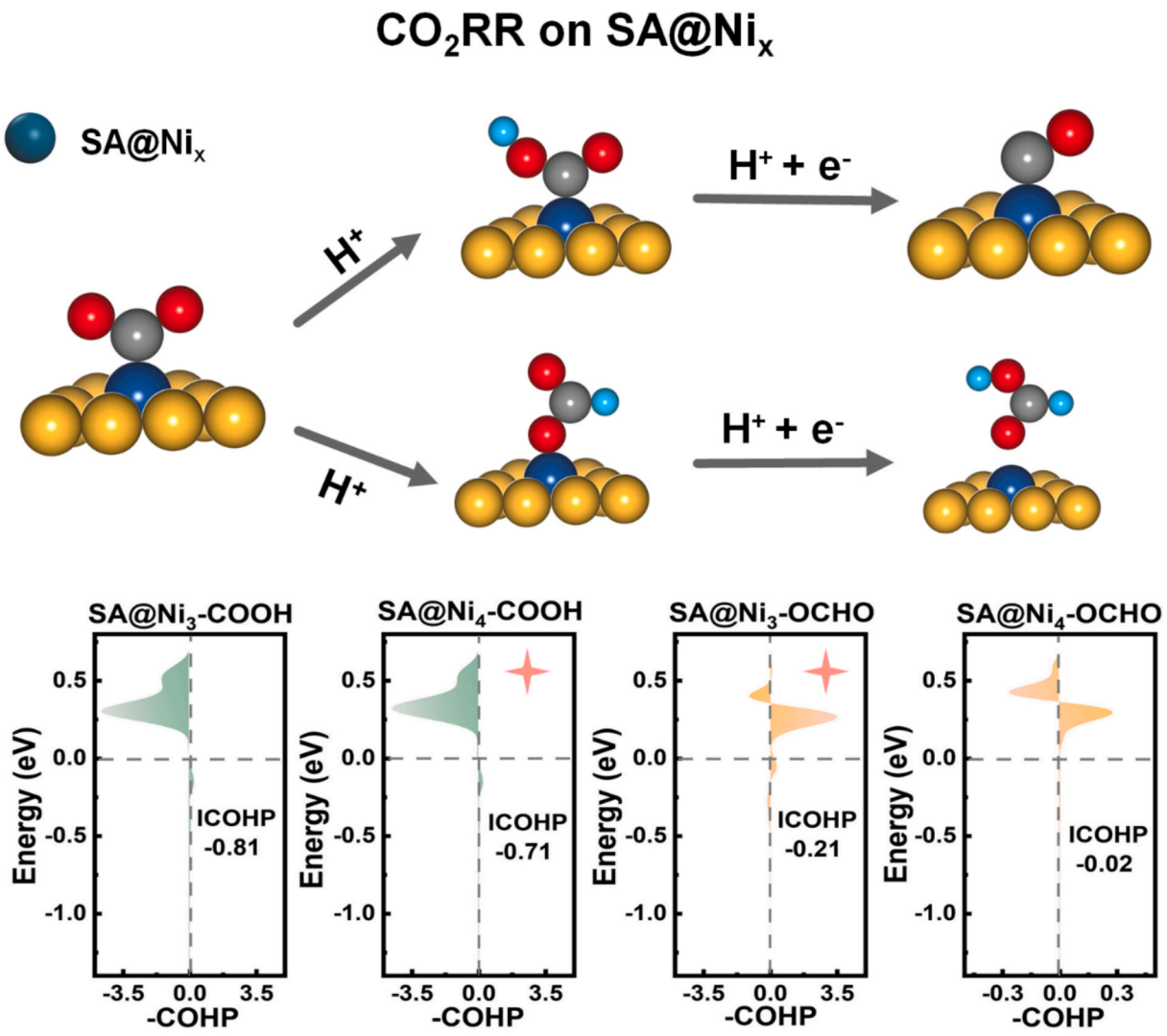

Fig. 6. ICOHP values for *COOH and *OCHO on SA@Ni_3 and SA@Ni_4, quantifying bond strength (more negative indicates stronger bonding). Ni_3 exhibits stronger *OCHO binding favoring HCOOH, while Ni_3 shows stronger *COOH binding favoring CO, consistent with their predicted product selectivity.

catalyst surface it is 0.64 eV. These results indicate that for CO production, the interaction strength between the *C of the *COOH intermediate and the Ni atoms in the SA@Ni_4 catalyst is moderate, thereby guaranteeing the optimal performance of the SA@Ni_4 catalyst in generating CO.

For HCOOH production, the ICOHP value on the SA@Ni_3 catalyst surface it is 0.21 eV, and on the SA@Ni_4 catalyst surface is 0.02 eV. As shown in **Figs. S7**, on the SA@Ni_1 catalyst surface, the ICOHP value the Ni–C interaction is 0.19 eV, on the SA@Ni_2 catalyst surface it is 0.23 eV, and on the SA@Ni_5 catalyst surface it is 0.22 eV. These results indicate that for HCOOH production, the interaction strength between the O atom in the OCHO intermediate and the Ni atoms in the SA@Ni_3 catalyst is moderate, thereby guaranteeing the optimal performance of the SA@Ni_3 catalyst in generating HCOOH. Furthermore, relying on on the corresponding relationship between the center of the d-band and the adsorption energy (Fig. 3 **a**), nickel cluster doping can optimize the position of the center of the d-band of the catalyst material.

Therefore, SA@Ni_4 and SA@Ni_3 have moderate adsorption energies for the key intermediates (COOH and OCHO), thereby demonstrating optimal catalytic performance. In conclusion, SA@Ni_4 and SA@Ni_3 are the best catalysts for the simultaneous production of CO and HCOOH.

The size-dependent selectivity advantages of SA@Ni_3 and SA@Ni_4 for CO_2RR are further supported by existing experimental studies on Ni-based catalysts, and the theoretical conclusions exhibit good consistency with experimental observations. The size-dependent product distribution (CO/HCOOH) predicted by DFT calculations is consistent with the catalytic behavior of Ni nanoparticle-single atom hybrid catalysts, where optimized Ni-N coordination can achieve a CO Faradaic efficiency (FE_{CO}) of up to 99.26% [74]. The predicted low overpotential range (0.5–0.66 V) for high selectivity is also in line with experimental reports, in which porous NiPNC catalysts maintain ~ 100% FE_{CO} at −0.8 to −1.1 V (vs. RHE) [75,76] and Ni_nN_x clusters exhibit FE_{CO} > 90% at −0.3 to −0.8 V (vs. RHE) [77]. In addition, the key role of Ni-N coordination emphasized in theoretical calculations is directly verified by XPS and XAFS characterizations, which confirm a positive correlation between Ni-N bond content and catalytic selectivity—for example, a 4.8-fold increase in Ni-N bond abundance can elevate FE_{CO} from < 60% to 98.6% [78].

Current experimental techniques cannot directly probe the atomic-scale electronic interactions and thermodynamic trends that determine catalytic selectivity, making DFT-derived quantitative parameters (d-band center, ICOHP, free energy barrier) indispensable for revealing the intrinsic catalytic mechanism. Theoretical models eliminate the interference of experimental variables such as pore structure and electrolyte composition, and accurately isolate the core cluster size-selectivity correlation to realize the quantitative interpretation of the CO_2RR

catalytic mechanism.

4. Conclusions

In conclusion, this DFT study systematically unravels the size-dependent catalytic behavior of carbon-supported Ni nanoclusters (SA@Ni_x, x = 1–5) for the CO_2RR. The SA@Ni_x configurations are confirmed to be structurally stable and metallically conductive, providing a robust foundation for electrocatalysis. Our calculations identify SA@Ni_4 and SA@Ni_3 as the most promising catalysts, which demonstrate high selectivity towards CO and HCOOH, respectively, while simultaneously suppressing the competing HER. The origin of this superior performance is deciphered through electronic structure analysis. The activity and selectivity of the catalyst are determined by the d-band center of the Ni site, and this d-band center is regulated by the cluster size. The adsorption strength of the key intermediates (COOH in the CO pathway and OCHO in the HCOOH pathway) was thus regulated to the optimal level, as further evidenced by COHP analysis. This work underscores the critical role of precise size regulation of cluster catalysts and establishes a fundamental theoretical framework that rational design of high-performance and high-selectivity electrocatalysts for CO_2 resource utilization. The structure–activity relationships elucidated herein may also provide generalizable guidance for optimizing coordination environments in other single-atom and cluster catalyst systems, fostering innovation in the broader field of electrocatalysis for sustainable energy and environmental applications.

CRediT authorship contribution statement

Yimeng Sun: Writing – original draft, Methodology, Investigation, Formal analysis, Data curation. **Lin Tao:** Writing – review & editing, Methodology, Funding acquisition, Formal analysis, Data curation, Conceptualization. **Meixu Lu:** Methodology, Investigation, Formal analysis. **Xin Quan:** Methodology, Investigation, Formal analysis. **Mingjie Wu:** Writing – review & editing, Methodology, Formal analysis, Conceptualization. **Javed Rehman:** Supervision, Methodology. **Nan Wang:** Writing – review & editing, Supervision, Formal analysis. **Lixiang Li:** Supervision, Resources, Formal analysis. **Baigang An:** Supervision, Formal analysis.

Declaration of competing interest

The authors declare that they have no known competing financial interests or personal relationships that could have appeared to influence the work reported in this paper.

Acknowledgment

The funding from the National Natural Science Foundation of China (Grant No. 52304330), the Natural Science Foundation of Liaoning Province (Grant No. 2024-BS-218), University of Science and Technology Liaoning Talent Project Grants (Grant No. 6003000317), the Outstanding Youth Fund of University of Science and Technology Liaoning (Grant No. 2023YQ11), and the Youth Fund of the Education Department of Liaoning Province (Grant No. LJKQZ20222324) are gratefully acknowledged.

Appendix A. Supplementary data

Supplementary data to this article can be found online at https://doi.org/10.1016/j.fuel.2026.139263.

Data availability

Data will be made available on request.

References

[1] Lu M, Tao L, Su Y, Sun Y, Dastan D, Rehman J, Zhang H, Zhao H, Li L, An B. First-principles study of bonding-driven selectivity in CO2 electroreduction on metal–nitrogen–carbon catalysts. J Phys Chem C 2025;130:326–35. https://doi.org/10.1021/acs.jpcc.5c07261.
[2] Sun Y, Tao L, Su Y, Dastan D, Zhang H, Zhao H, Li L, An B. Emerging two-dimensional supported atomic and cluster catalysts for CO2 electroreduction. Nanoscale Horiz 2026. https://doi.org/10.1039/D5NH00710K.
[3] Tao L, Huang J, Dastan D, Wang T, Li J, Yin X, Wang Q. New insight into absorption characteristics of CO2 on the surface of calcite, dolomite, and magnesite. Appl Surf Sci 2021;540:148320. https://doi.org/10.1016/j.apsusc.2020.14832.
[4] Nie S, Tao L, Yu H, Dastan D, Wang W, Hong L, Li L, An B, Su Y. Theoretical and machine learning exploration of electronic factors governing Ni-centered CO2 reduction catalysts. Phys Chem Chem Phys 2025;27:21810–23. https://doi.org/10.1039/D5CP02458G.
[5] Pu M, Guo W, Guo Y. Non-Noble Metal Incorporated transition Metal Dichalcogenide Monolayers for Electrochemical CO(2) Reduction: a First-Principles Study. ACS Appl Mater Interfaces 2023;15(50):58388–96. https://doi.org/10.1021/acsami.3c13240.
[6] Qin R, Liu K, Wu Q, Zheng N. Surface Coordination Chemistry of Atomically Dispersed Metal Catalysts. Chem Rev 2020;120(21):11810–99. https://doi.org/10.1021/acs.chemrev.0c00094.
[7] Lu B, Liu Q, Chen S. Electrocatalysis of Single-Atom Sites: Impacts of Atomic Coordination. ACS Catal 2020;10(14):7584–618. https://doi.org/10.1021/acscatal.0c01950.
[8] Wu M, Yang S, Gao Y, Chen Z, Dong F, Lei H, et al. Steering CO2 Electroreduction Pathway via Tuning Microenvironment of Cobalt Center in Molecular Catalysts. ACS Nano 2025;19(36):32507–17. https://doi.org/10.1021/acsnano.5c09554.
[9] Tuo J, Zhu Y, Cheng L, Li Y, Yang X, Shen J, et al. Layered Confinement Reaction: Atomic-level Dispersed Iron–Nitrogen Co-Doped Ultrathin Carbon Nanosheets for CO2 Electroreduction. ChemSusChem 2019;12(12):2644–50. https://doi.org/10.1002/cssc.201901058.
[10] Ju W, Bagger A, Hao G-P, Varela AS, Sinev I, Bon V, et al. Understanding activity and selectivity of metal-nitrogen-doped carbon catalysts for electrochemical reduction of CO2. Nat Commun 2017;8(1):944. https://doi.org/10.1038/s41467-017-01035-z.
[11] Li X, Bi W, Chen M, Sun Y, Ju H, Yan W, et al. Exclusive Ni–N4 Sites Realize Near-Unity CO Selectivity for Electrochemical CO2 Reduction. J Am Chem Soc 2017;139(42):14889–92. https://doi.org/10.1021/jacs.7b09074.
[12] Möller T, Ju W, Bagger A, Wang X, Luo F, Ngo Thanh T, et al. Efficient CO2 to CO electrolysis on solid Ni–N–C catalysts at industrial current densities. Energ Environ Sci 2019;12(2):640–7. https://doi.org/10.1039/C8EE02662A.
[13] He Q, Lee JH, Liu D, Liu Y, Lin Z, Xie Z, et al. Accelerating CO2 electroreduction to CO over Pd Single-Atom Catalyst. Adv Funct Mater 2020;30(17):2000407. https://doi.org/10.1002/adfm.202000407.
[14] Geng Z, Cao Y, Chen W, Kong X, Liu Y, Yao T, et al. Regulating the coordination environment of Co single atoms for achieving efficient electrocatalytic activity in CO2 reduction. Appl Catal B 2019;240:234–40. https://doi.org/10.1016/j.apcatb.2018.08.075.
[15] Zhang Y, Jiao L, Yang W, Xie C, Jiang H-L. Rational Fabrication of Low-Coordinate Single-Atom Ni Electrocatalysts by MOFs for Highly Selective CO2 Reduction. Angew Chem Int Ed 2021;60(14):7607–11. https://doi.org/10.1002/anie.202016219.
[16] Pu M, Guo W, Guo Y. Non-Noble Metal Incorporated transition Metal Dichalcogenide Monolayers for Electrochemical CO2 Reduction: a First-Principles Study. ACS Appl Mater Interfaces 2023;15(50):58388–96. https://doi.org/10.1021/acsami.3c13240.
[17] McCarver GA, Yildirim T, Zhou W. Hetero-bimetallic paddlewheel complexes for enhanced CO2 reduction selectivity in MOFs: a first principles study. PCCP 2024;26(9):7627–37. https://doi.org/10.1039/D3CP05694E.
[18] Xing G, Liu S, Liu J-y. Two-dimensional metal–organic frameworks with dual active sites for electrochemical CO2 reduction: a computational study. Sep Purif Technol 2025;361:131275. https://doi.org/10.1016/j.seppur.2024.131275.
[19] Astruc D. Introduction: Nanoparticles in Catalysis. Chem Rev 2020;120(2):461–3. https://doi.org/10.1021/acs.chemrev.8b00696.
[20] Tyo EC, Vajda S. Catalysis by clusters with precise numbers of atoms. Nat Nanotechnol 2015;10(7):577–88. https://doi.org/10.1038/nnano.2015.140.
[21] Chakraborty I, Pradeep T. Atomically Precise Clusters of Noble Metals: Emerging link between Atoms and Nanoparticles. Chem Rev 2017;117(12):8208–71. https://doi.org/10.1021/acs.chemrev.6b00769.
[22] Li F, MacFarlane DR, Zhang J. Recent advances in the nanoengineering of electrocatalysts for CO2 reduction. Nanoscale 2018;10(14):6235–60. https://doi.org/10.1039/C7NR09620H.
[23] Liu L, Corma A. Metal Catalysts for Heterogeneous Catalysis: from Single Atoms to Nanoclusters and Nanoparticles. Chem Rev 2018;118(10):4981–5079. https://doi.org/10.1021/acs.chemrev.7b00776.
[24] Munir A, Joya KS, Ulhaq T, Babar N-U-A, Hussain SZ, Qurashi A, et al. Metal Nanoclusters: New Paradigm in Catalysis for Water Splitting, Solar and Chemical Energy Conversion. ChemSusChem 2019;12(8):1517-48. Doi: 10.1002/cssc.201802069.
[25] Zhao S, Jin R, Jin R. Opportunities and challenges in CO2 Reduction by Gold- and Silver-based Electrocatalysts: from Bulk Metals to Nanoparticles and Atomically Precise Nanoclusters. ACS Energy Lett 2018;3(2):452–62. https://doi.org/10.1021/acsenergylett.7b01104.

[26] Kwak K, Lee D. Electrochemistry of Atomically Precise Metal Nanoclusters. Acc Chem Res 2019;52(1):12–22. https://doi.org/10.1021/acs.accounts.8b00379.
[27] Kumar B, Kawawaki T, Shimizu N, Imai Y, Suzuki D, Hossain S, et al. Gold nanoclusters as electrocatalysts: size, ligands, heteroatom doping, and charge dependences. Nanoscale 2020;12(18):9969–79. https://doi.org/10.1039/D0NR00702A.
[28] Jin R, Zeng C, Zhou M, Chen Y. Atomically Precise Colloidal Metal Nanoclusters and Nanoparticles: Fundamentals and Opportunities. Chem Rev 2016;116(18):10346–413. https://doi.org/10.1021/acs.chemrev.5b00703.
[29] Jin R. Quantum sized, thiolate-protected gold nanoclusters. Nanoscale 2010;2(3):343–62. https://doi.org/10.1039/B9NR00160C.
[30] Wei J, Ya H-L, Qin S-N, Zhang H, Tian Z-Q, Li J-F. Efficient CO2 electroreduction on Pd-based core-shell nanostructure with tensile strain. J Electroanal Chem 2021;896:115205. https://doi.org/10.1016/j.jelechem.2021.115205.
[31] Chang Y-B, Zhang C, Lu X-L, Zhang W, Lu T-B. Graphdiyene enables ultrafine Cu nanoparticles to selectively reduce CO2 to C2+ products. Nano Res 2022;15(1):195–201. https://doi.org/10.1007/s12274-021-3456-2.
[32] Zhu Z, Li Z, Wei X, Wang J, Xiao S, Li R, et al. Achieving efficient electroreduction of CO2 to CO in a wide potential window by encapsulating Ni nanoparticles in N-doped carbon nanotubes. Carbon 2021;185:9–16. https://doi.org/10.1016/j.carbon.2021.08.072.
[33] Li Y, Chen C, Cao R, Pan Z, He H, Zhou K. Dual-atom Ag2/graphene catalyst for efficient electroreduction of CO2 to CO. Appl Catal B 2020;268:118747. https://doi.org/10.1016/j.apcatb.2020.118747.
[34] Ma X, Tian J, Wang M, Shen M, Zhang L. Polymeric carbon nitride supported Bi nanoparticles as highly efficient CO2 reduction electrocatalyst in a wide potential range. J Colloid Interface Sci 2022;608:1676–84. https://doi.org/10.1016/j.jcis.2021.10.049.
[35] Ávila-Bolívar B, Montiel V, Solla-Gullón J. On the activity and stability of Sb2O3/Sb nanoparticles for the electroreduction of CO2 toward formate. J Electroanal Chem 2021;895:115440. https://doi.org/10.1016/j.jelechem.2021.115440.
[36] Duan Y-X, Liu K-H, Zhang Q, Yan J-M, Jiang Q. Efficient CO2 Reduction to HCOOH with High Selectivity and Energy Efficiency over Bi/rGO Catalyst. Small Methods 2020;4(5):1900846. https://doi.org/10.1002/smtd.201900846.
[37] Boppella R, Kim Y, Joshi Reddy KA, Song I, Eom Y, Sim E, et al. Synergistic electronic structure modulation in single-atomic Ni sites dispersed on Ni nanoparticles encapsulated in N-rich carbon nanotubes synthesized at low temperature for efficient CO2 electrolysis. Appl Catal B Environ 2024;345:123699. https://doi.org/10.1016/j.apcatb.2024.123699.
[38] Zhang S, Tao L, Zhang H, Zhao H, Di F, Li L, An B. Theoretical study of metal-doped WSe2 sensors for NO detection in human exhalation. Surf Interfaces 2025;73:107553. https://doi.org/10.1016/j.surfin.2025.107553.
[39] Gu M, Tao L, Dastan D, Dang J, Fang T, An B. Metal-modified C3N1 monolayer sensors for battery instability monitoring. J Mater Chem A 2024;12:15254–64. https://doi.org/10.1039/d4ta00645c.
[40] Zhang H, Lei H, Xiao Y, Wang G, Zhang D. Atomic-scale nucleation pathways of MgAl2O4 particle in molten steel. Comput Theor Chem 2024;1234:114544. https://doi.org/10.1016/j.comptc.2024.114544.
[41] Gu M, Tao L, Dastan D, Dang J, Zhang X, Li L, An B. Metal-enhanced carbon-nitrogen material for selective detection of hazardous gases: Insights from interface electronic states. Surf Interfaces 2024;53:105097. https://doi.org/10.1016/j.surfin.2024.105097.
[42] Song C, Tao L, Dang J, Dastan D, Wang W, Zhang X, Li L, An B. Tuning NO2 selectivity in MoSe2 sensors via metal modification: Fermi-level electronic state control. Comput Theor Chem 2025;1250:115296. https://doi.org/10.1016/j.comptc.2025.115296.
[43] Tawalbeh M, Javed RMN, Al-Othman A, Almomani F, Ajith S. Unlocking the potential of CO2 hydrogenation into valuable products using noble metal catalysts: a comprehensive review. Environ Technol Innovation 2023;31:103217. https://doi.org/10.1016/j.eti.2023.103217.
[44] Ms. Maksuda Khatun DTR, Dr. Debadrita Roy, Dr. Nitish Roy, Prof. Mahendra Nath Roy. Adsorption and Activation of CO2 on the Surface of Nin Clusters (n=2 to 6, 8): An Insight from DFT study. International Journal on Science and Technology 2025;16(3). Doi: 10.71097/IJSAT.v16.i3.8368.
[45] Sanwal P, Raza A, Miao Y-X, Lumbers B, Li G. Advances in coinage metal nanoclusters: from synthesis strategies to electrocatalytic performance. Polyoxometalates 2024;3(3):9140057. https://doi.org/10.26599/POM.2024.9140057.
[46] Denos X, Alfonso D, Nguyen-Phan T-D, Kauffman DR. Breaking the Limit of Size-Dependent CO2RR Selectivity in Silver Nanoparticle Electrocatalysts through Electronic Metal–Carbon Interactions. ACS Catal 2023;13(23):15301–9. https://doi.org/10.1021/acscatal.3c03446.
[47] Guo Y, Zhang L, Zou Y, Wang X, Ning Q. Graphene-Supported Cun (n = 5, 6) Clusters for CO2 Reduction Catalysis. Nanomaterials 2025;15(6):445. https://doi.org/10.3390/nano15060445.
[48] Pan Q, Chen Y, Li H, Ma G, Jiang S, Cui X, et al. Size effect of nickel from nanoparticles to clusters to single atoms for electrochemical CO2 reduction. J Mater Chem A 2024;12(31):20035–44. https://doi.org/10.1039/D4TA03404J.
[49] Wang F, Meng Y, Chen X, Zhang L, Li G, Shen Z, et al. Effect of nickel-based electrocatalyst size on electrochemical carbon dioxide reduction: a density functional theory study. J Colloid Interface Sci 2022;615:587–96. https://doi.org/10.1016/j.jcis.2022.02.032.
[50] Ma Q, Zhu H, Liu D, Li R, Li T, Ren H, et al. Identifying magic-number structures of supported sub-nano Ni clusters and the influence of hydrogen coverage: a density functional theory based particle swarm optimization investigation. Cat Sci Technol 2023;13(7):2080–91. https://doi.org/10.1039/D3CY00037K.
[51] de Lara-Castells MP. An Ab Initio Journey toward the Molecular-Level Understanding and Predictability of Subnanometric Metal Clusters. Small Struct 2024;5(10). https://doi.org/10.1002/sstr.202470048.
[52] Peng W, Li F, Kong S, Guo C, Wu H, Wang J, et al. Recent advances in nickel-based catalysts in eCO2RR for carbon neutrality. Carbon Energy 2024;6(2). https://doi.org/10.1002/cey2.498.
[53] Delley B. From molecules to solids with the DMol3 approach. J Chem Phys 2000;113(18):7756–64. https://doi.org/10.1063/1.1316015.
[54] Louie SG, Chan Y-H, da Jornada FH, Li Z, Qiu DY. Discovering and understanding materials through computation. Nat Mater 2021;20(6):728–35. https://doi.org/10.1038/s41563-021-01015-1.
[55] Tkatchenko A, Scheffler M. Accurate molecular van der Waals interactions from ground-state electron density and free-atom reference data. Phys Rev Lett 2009;102(7):073005. https://doi.org/10.1103/PhysRevLett.102.073005.
[56] Zhang S, Tao L, Fang T, Dang J, Dastan D, Li L, An B. Resolving competitive adsorption pathways on Ir-WSe2 nanosheets via DFT simulations for ultra-selective no recognition in harsh environments. ACS Appl Nano Mater 2026;9:4367–77. https://doi.org/10.1021/acsanm.6c00150.
[57] Grimme S. Semiempirical GGA-type density functional constructed with a long-range dispersion correction. J Comput Chem 2006;27(15):1787–99. https://doi.org/10.1002/jcc.20495.
[58] Nie S, Tao L, Li J, Wang W, Poldorn P, He Y, et al. A single response to reducing gases by NiO-TiO2 heterojunction nanocrystals. Appl Surf Sci 2024;644:158821. https://doi.org/10.1016/j.apsusc.2023.158821.
[59] He Y, Tao L, Li J, Wu M, Poldorn P, Dastan D, et al. Atomic-level insights into selective adsorption of H2 and CO on SnO2/CoO heterojunctions. Mater Today Nano 2023;22:100334. https://doi.org/10.1016/j.mtnano.2023.100334.
[60] Tao L, Huang J, Dastan D, Wang T, Li J, Yin X, et al. CO2 capture and separation on charge-modulated calcite. Appl Surf Sci 2020;530:147265. https://doi.org/10.1016/j.apsusc.2020.147265.
[61] Tao L, Dastan D, Wang W, Poldorn P, Meng X, Wu M, et al. Metal-decorated InN Monolayer Senses N2 against CO2. ACS Appl Mater Interfaces 2023;15(9):12534–44. https://doi.org/10.1021/acsami.2c21463.
[62] Pedersen PD, Melander MM, Bligaard T, Vegge T, Honkala K, Hansen HA. Grand Canonical DFT Investigation of the CO2RR and HER Reaction Mechanisms on MoTe2 Edges. J Phys Chem C 2023;127(38):18855–64. https://doi.org/10.1021/acs.jpcc.3c04474.
[63] Wang M, Ma W, Tan C, Qiu Z, Hu L, Lv X, et al. Designing efficient non-precious metal electrocatalysts for high-performance hydrogen production: A comprehensive evaluation strategy. Small 2023:e2306631. https://doi.org/10.1002/smll.202306631.
[64] He Y, Li J, Tao L, Nie S, Fang T, Yin X, et al. First-principles calculations on the resistance and electronic properties of H2 adsorption on a CoO-SnO2 heterojunction surface. PCCP 2021;24(1):392–402. https://doi.org/10.1039/D1CP04539C.
[65] Wu H, Zhang G, Cui H, Deng X. Atomic-level sensing mechanism of Rh-doped MoS2-WS2 heterojunction towards dissolved H2, C2H2, and C2H4 in transformer oil: A first-principles study. Colloids Surf A: Physicochem Eng Asp 2026;738:140006. https://doi.org/10.1016/j.colsurfa.2026.140006.
[66] Tao L, Huang J, Yin X, Wang Q, Li Z, Wang G, et al. Adsorption Kinetics of CO2 on a Reconstructed Calcite Surface: an Experiment-simulation Collaborative Method. Energy Fuels 2019;33(9):8946–53. https://doi.org/10.1021/acs.energyfuels.9b01771.
[67] Tao L, Huang J, Dastan D, Li J, Yin X, Wang Q. Flue gas separation at organic-inorganic interface under geological conditions. Surf Interfaces 2021;27:101462. https://doi.org/10.1016/j.surfin.2021.101462.
[68] Wu J, Wu D, Li H, Song Y, Lv W, Yu X, et al. Tailoring the coordination environment of double-atom catalysts to boost electrocatalytic nitrogen reduction: a first-principles study. Nanoscale 2023;15(39):16056–67. https://doi.org/10.1039/D3NR03310D.
[69] Wang Y-Q, Dan X-H, Yi Z-Y, Wang X, Feng Y-C, Feng Y, et al. Single-Molecule Study on the Catalytic Role of Co–O2 Binding in ORR by In Situ ECSTM. J Phys Chem C 2023;127(6):2929–35. https://doi.org/10.1021/acs.jpcc.2c07891.
[70] Zhang X, Tao L, Dastan D, Zhang H, Gao B. Tuning the electrochemical stability of carbon based single-atom structures via doping: trade-off between electrosorption/leaching behavior. J. Mater. Chem. A. 2025;13:23715–23. https://doi.org/10.1039/d5ta03307a.
[71] Zhang S, Tao L, Fang T, Dang J, Dastan D, Li L, An B. Battery fault NO2 detection using Au/Pt-modified MoSe2: A DFT study. Colloids Surf A: Physicochem Eng Asp 2026;740:140214. https://doi.org/10.1016/j.colsurfa.2026.140214.
[72] Zhang Z, Tao L, Quan X, Gu M, Zhang H, An B, Li L. Regulating the H2 selectivity of MoS2 sensors through synergistic metal–non-metal co-doping. Mater Sci Semicond Process 2026;206:110460. https://doi.org/10.1016/j.mssp.2026.110460.
[73] Sun Y, Tao L, Wu M, Dastan D, Rehman J, Li L, et al. Multi-atomic loaded C2N1 catalysts for CO2 reduction to CO or formic acid. Nanoscale 2024;16(20):9791–801. https://doi.org/10.1039/D4NR01082E.
[74] Wang C, Chen B, Ren H, Wang X, Li W, Hu H, et al. Stabilizing Ni single-atom sites through introducing low-valence Ni Species for durably efficient electrochemical CO2 reduction. Appl Catal B Environ 2025;368:125151. https://doi.org/10.1016/j.apcatb.2025.125151.
[75] Bai W, Xiao L, Cheng G, Ma J, Chang F, Guo C, et al. Porous nitrogen-doped carbon anchored with highly dispersed nickel active sites for efficient carbon dioxide electroreduction. Mater Today Commun 2025;45:112197. https://doi.org/10.1016/j.mtcomm.2025.112197.

[76] Zhang M, Wu T-S, Hong S, Fan Q, Soo Y-L, Masa J, et al. Efficient Electrochemical Reduction of CO2 by Ni–N Catalysts with Tunable Performance. ACS Sustain Chem Eng 2019;7(17):15030–5. https://doi.org/10.1021/acssuschemeng.9b03502.
[77] Ma X, Xu X, Geng L, Si J, Song Z, Wang W, et al. Nitrogen imported in nickel clusters promotes carbon dioxide electrochemical reduction to carbon monoxide. J Colloid Interface Sci 2025;689:137255. https://doi.org/10.1016/j.jcis.2025.137255.
[78] Xu G, Peng X, Wu C, Xi S, Xiang H, Feng L, et al. Atomically precise Ni clusters inducing active NiN2 sites with uniform-large vacancies towards efficient CO2-to-CO conversion. Nat Commun 2025;16(1). https://doi.org/10.1038/s41467-025-59079-5.